



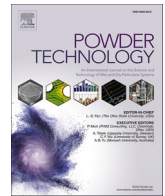
## Effect of layer thickness on spatters oxidation of Hastelloy X alloy during powder bed fusion-laser beam processing

Downloaded from: <https://research.chalmers.se>, 2024-03-20 11:41 UTC

Citation for the original published paper (version of record):

Raza, A., de Andrade Schwerz, C., Pauzon, C. et al (2023). Effect of layer thickness on spatters oxidation of Hastelloy X alloy during powder bed fusion-laser beam processing. Powder Technology, 422.  
<http://dx.doi.org/10.1016/j.powtec.2023.118461>

N.B. When citing this work, cite the original published paper.



# Effect of layer thickness on spatters oxidation of Hastelloy X alloy during powder bed fusion-laser beam processing

Ahmad Raza<sup>a,\*</sup>, Claudia Schwerz<sup>a</sup>, Camille Pauzon<sup>a,b</sup>, Lars Nyborg<sup>a</sup>, Eduard Hryha<sup>a</sup>

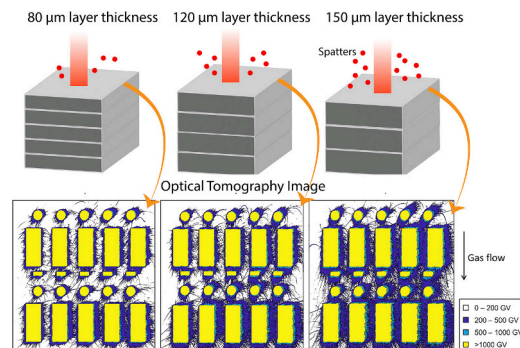
<sup>a</sup> Chalmers University of Technology, Department of Industrial and Materials Science, SE-41296 Göteborg, Sweden

<sup>b</sup> Université Grenoble Alpes, CNRS, Grenoble INP, SIMaP, 38000, Grenoble, France

## HIGHLIGHTS

- The OT analysis showed an increase in the number of spatters signals with the increase in powder layer thickness.
- The number of redeposited spatters on the powder bed also increased with the increase in powder layer thickness.
- The morphology analysis showed that not all spatters oxidize in a similar fashion.
- The chemistry of oxides on the spatter surface varied by the changes in the morphology of the spatters.
- Spatters from 150  $\mu\text{m}$  powder layer thickness showed the highest oxide particulate thickness.

## GRAPHICAL ABSTRACT



## ARTICLE INFO

### Keywords:

In-situ monitoring  
Spatters formation  
Oxidation  
XPS  
AES

## ABSTRACT

This study investigates the impact of powder layer thickness on spatter generation and oxidation behavior during the processing of Hastelloy X. In-situ monitoring using optical tomography reveals that thicker powder layers result in a higher number of hot spatters generated during laser-melt-powder interaction. Scanning electron microscopy and Auger electron spectroscopy analysis demonstrate the presence of different types of spatters that oxidize differently depending on their origin. X-ray photoelectron spectroscopy analysis further shows that the surface enrichment of oxide-forming elements such as Al, Ti, Cr, and Fe varies with the type of spatter particle. Additionally, depth profile analysis using X-ray photoelectron spectroscopy indicates that the average oxide layer thickness increases from  $\sim 2.5$  nm in virgin to  $\sim 68$  nm in spatters generated at 150  $\mu\text{m}$  powder layer thickness. The findings suggest that powder layer thickness is a crucial factor in controlling spatter generation and oxidation behavior during powder bed fusion-laser beam processing.

## 1. Introduction

As an emerging technology in production, additive manufacturing still faces multiple challenges for wide adaption in the industry. One of

these challenges is the low productivity of the AM techniques, particularly powder bed fusion-laser beam (PBF-LB), which makes the process expensive and less viable manufacturing route compared to conventional processes [1]. To increase productivity, multidimensional

\* Corresponding author.

E-mail address: [ahmadra@chalmers.se](mailto:ahmadra@chalmers.se) (A. Raza).

<https://doi.org/10.1016/j.powtec.2023.118461>

Received 7 February 2023; Received in revised form 16 March 2023; Accepted 17 March 2023

Available online 22 March 2023

0032-5910/© 2023 The Authors. Published by Elsevier B.V. This is an open access article under the CC BY license (<http://creativecommons.org/licenses/by/4.0/>).

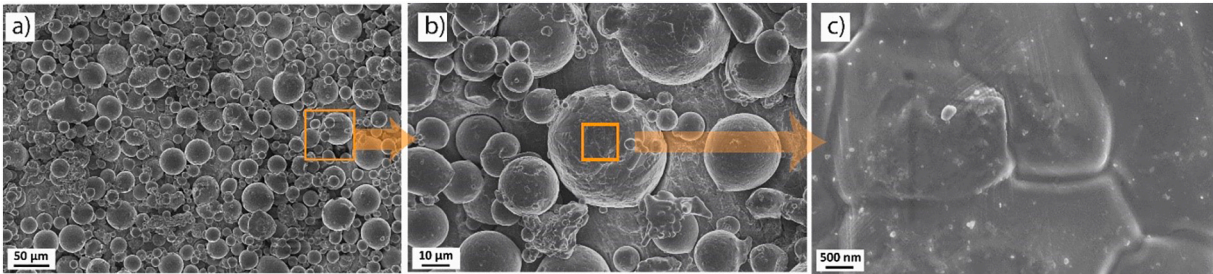


Fig. 1. Morphology of virgin powder at different magnifications observed through HR-SEM.

Table 1  
Composition of HX alloy provided by the manufacturer.

Element	Ni	Cr	Fe	Mo	W	Co	Si	Al	Ti
Wt%	Balance	20.88	17.35	8.68	0.81	1.44	0.2	0.05	0.07

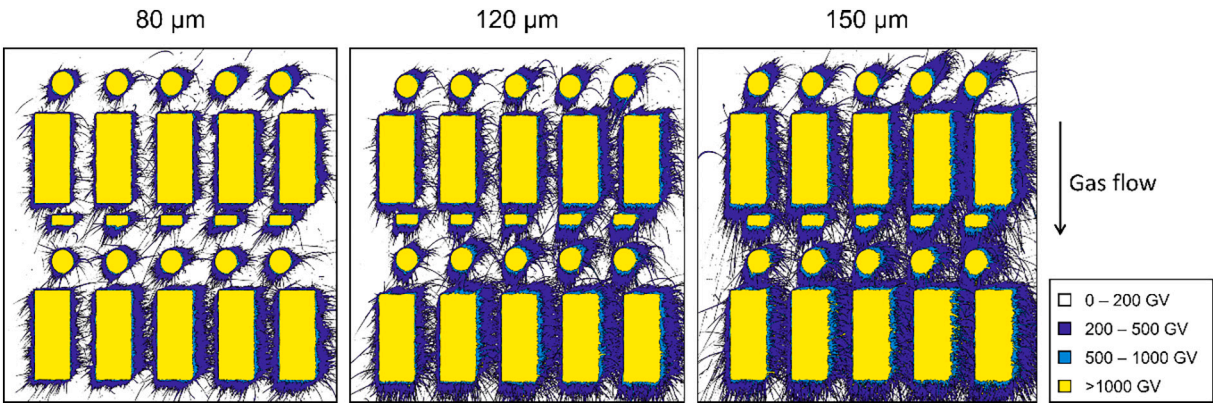


Fig. 2. Contour plots of the signal intensity registered via OT of a single representative layer of builds performed with nominal layer thicknesses 80 μm, 120 μm, and 150 μm.

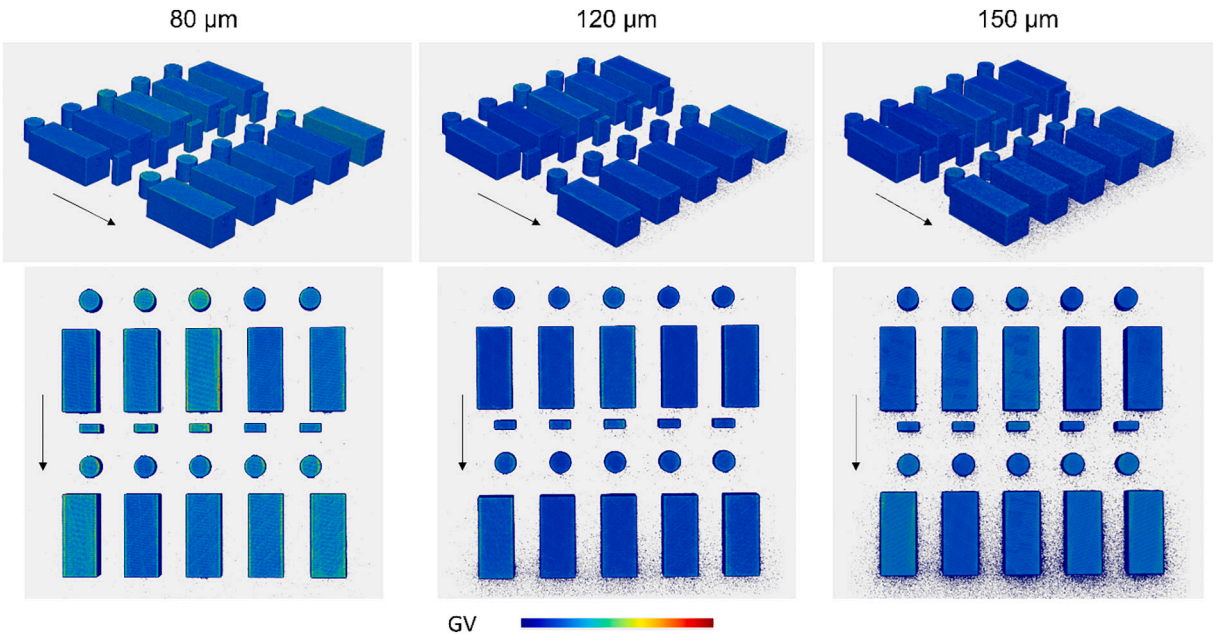
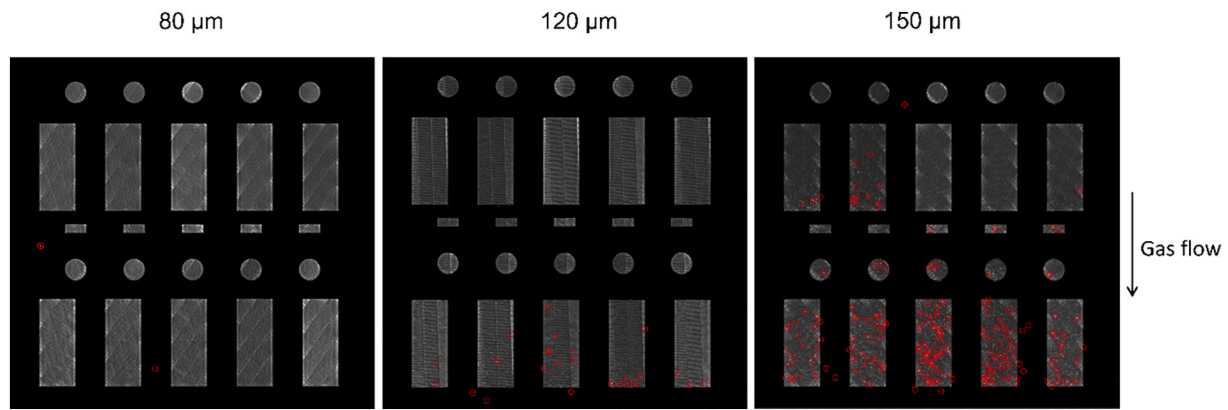
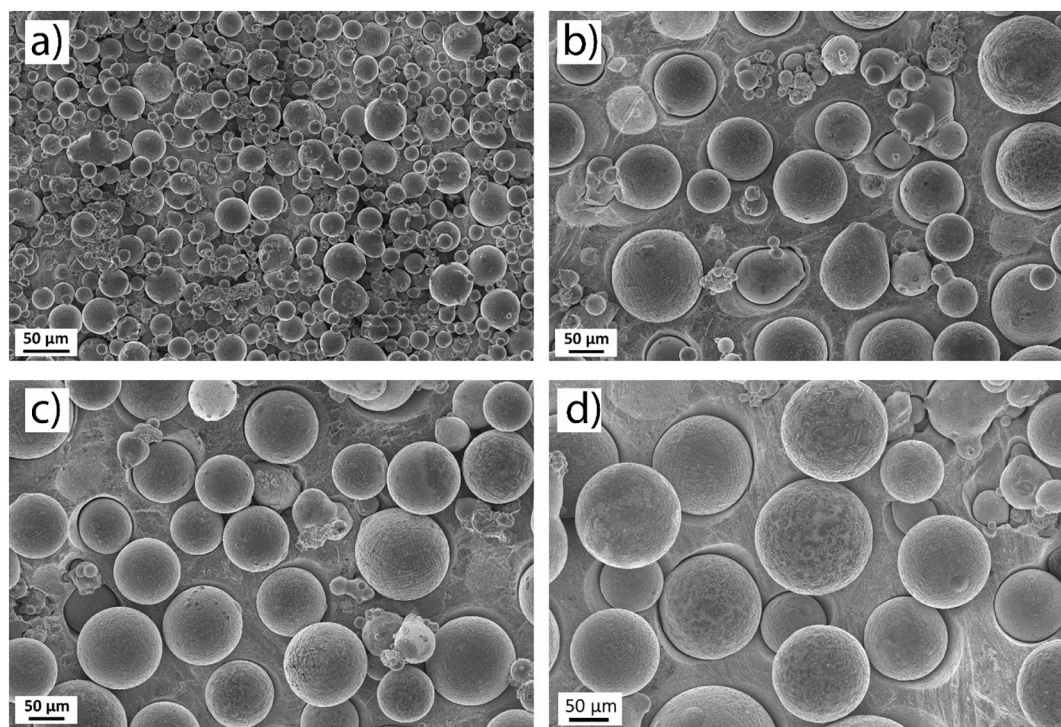


Fig. 3. Isometric and top view 3D reconstruction of the builds performed at nominal layer thicknesses 80 μm, 120 μm, and 150 μm. The intensity is represented according to the colormap indicated and the opacity is proportional to the intensity in the volume rendering. The direction of gas flow is indicated by black arrows.





**Fig. 4.** Sample representative OT images of builds performed with nominal layer thicknesses 80  $\mu\text{m}$ , 120  $\mu\text{m}$ , and 150  $\mu\text{m}$  overlaid with spatter detections encircled in red. (For interpretation of the references to color in this figure legend, the reader is referred to the web version of this article.)



**Fig. 5.** Morphology comparison of a) virgin powder with spatter samples obtained at a layer thickness of b) 80  $\mu\text{m}$ , c) 120  $\mu\text{m}$ , and d) 150  $\mu\text{m}$ .

research has been conducted where many modifications have been implemented in machines' hardware and process parameters.

Among process parameters, hatch distance, scan speed, and layer thickness are the parameters that can be modified to increase the build rate of the process [2,3]. The hatch distance and scan speed have a rational function with the build rate where the functions asymptote horizontally suggesting that the build rate cannot be indefinitely increased using these parameters [4]. However, the layer thickness has a linear function with the build rate which provides more space to increase the build rate and productivity [7]. Several researchers have investigated the effect of layer thickness on the tensile properties of the parts and found a minimal effect of an increase in layer thickness on the static mechanical strength [2,5,6]. Whereas a few researchers have reported that the increase in powder layer thickness leads to melt pool flow instability by affecting the recoil pressure and Marangoni flow [7]. Such melt pool instability can cause defect formation and spatters generation, which can affect both the quality of parts and the state of unconsumed powder.

Spatters are unwanted by-products of powder bed fusion techniques generated by the laser-melt-powder interaction [8,9]. Depending upon their temperature, the spatters interact with the residual oxygen present in the build chamber and oxidize [10]. The resultant extent of oxidation depends upon the residual oxygen content, alloying constituents, build chamber atmosphere, and temperature of spatter particles [11]. The conservation upon recycling of such oxidized spatter particles in the powder bed or redeposition over the subsequent parts can cause defect formation which can affect the reproducibility of the parts. One such study was conducted by Schwerz et al. [12] on Hastelloy X alloy, where the effect of spatter redeposition on the subsequent parts was investigated. The results showed the formation of a lack of fusion defect on the site of spatters deposition. Such defects occurred due to the presence of thick oxide on the surface of spatter particles and the relatively larger size of spatters compared to feedstock powder which led to low laser absorption, higher melting temperature, and a larger volume to melt. Furthermore, the study also correlated the effect of the number of generated spatters with the layer thickness of the powder and showed

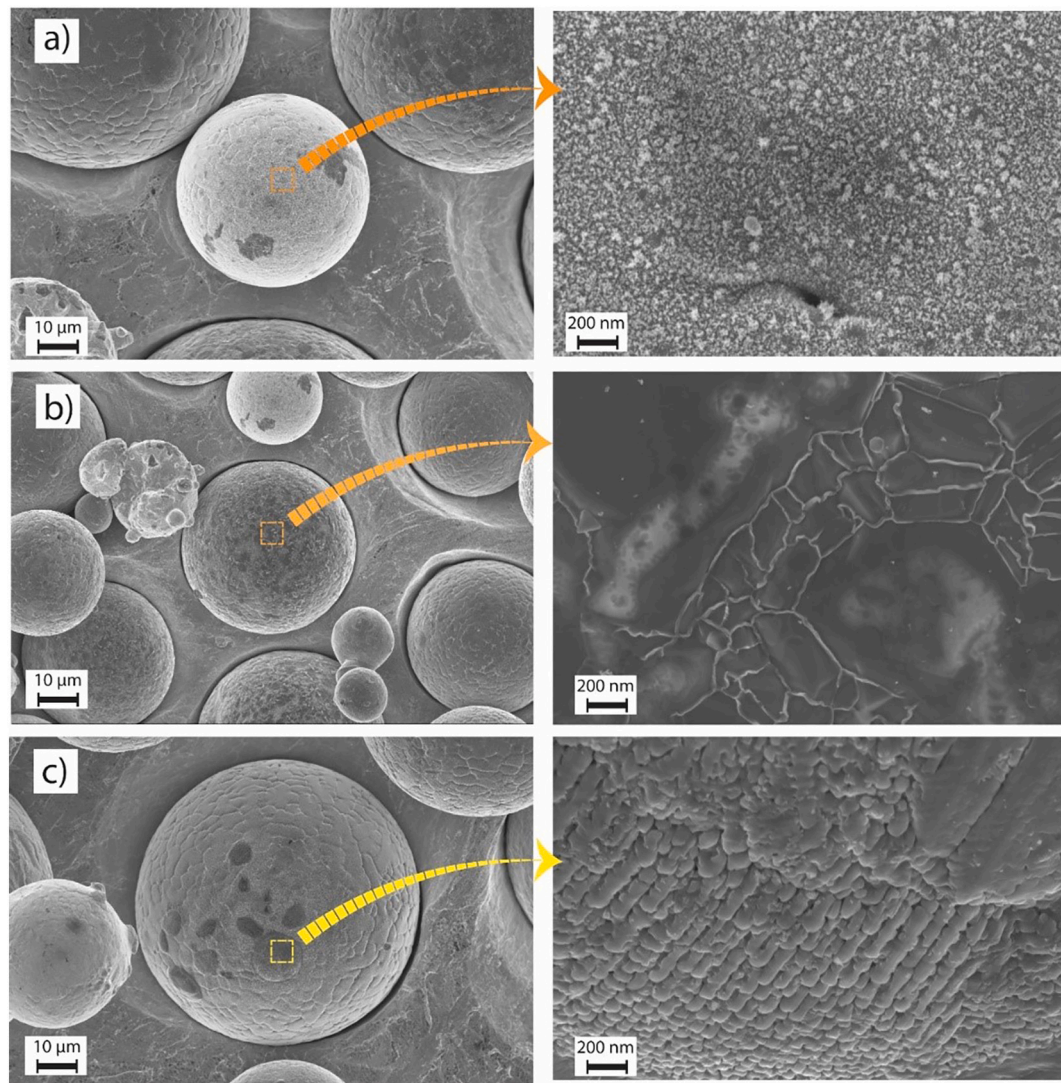


Fig. 6. Comparison of surface morphology of different spatter particles.

that the number of generated spatters increased with an increase in the powder layer thickness. This increase in spatter generation relates to the increase in melt-pool instability with the increment of powder layer thickness [7].

This study aims to analyze spatter particles and investigate the effect of varying powder layer thickness (80  $\mu\text{m}$ , 120  $\mu\text{m}$ , and 150  $\mu\text{m}$ ) on the number of spatters, their oxidation behavior, nature, and thickness of oxides during the processing of Hastelloy X alloy. The characterization of spatter morphology was performed using high-resolution scanning and transmission electron microscopy. Additionally, the surface composition was determined using Auger electron spectroscopy and X-ray photoelectron spectroscopy. The findings reveal new insights into the properties of Hastelloy X spatters and the impact of layer thickness. The study aims to demonstrate the relationship between higher productivity and unconsumed powder health by investigating the variation in the nature and thickness of oxide layers with varying layer thickness.

## 2. Materials and methods

Gas atomized Hastelloy X (HX) powder with the particle size distribution of 19  $\mu\text{m}$  (D10), 35  $\mu\text{m}$  (D50), and 58  $\mu\text{m}$  (D90), supplied by EOS GmbH (Electro-Optical System), is used as a feedstock material for this study. The powder has a spherical morphology with the presence of some satellites attached to the surface of the particles, see Fig. 1. The

high magnification imaging in Fig. 1c shows a rather clean surface with some particulate nucleation and dendrites present on the surface. The composition of the alloy is listed in Table 1 where it can be observed that the content of elements susceptible to oxidation, e.g., Al, Ti, is very low except for Cr.

The HX alloy powder was processed in an EOS M290 machine, and spatter samples were collected from a gas outlet. The collection of samples from the gas outlet and their identification as spatters was clarified in our previous work [10]. To investigate the role of powder layer thickness on spatter oxidation, three builds were done by using nominal layer thicknesses of 80  $\mu\text{m}$ , 120  $\mu\text{m}$ , and 150  $\mu\text{m}$ . To get fully dense material, the process parameters were optimized according to the procedure described in [12], and consisted of laser power of 370 W, a scan speed of 900 mm/s, and hatch spacing of 100  $\mu\text{m}$ . Micrographs of specimens manufactured in these conditions can be seen in Fig. 1 in the Appendix, where the measured defect content is also presented and does not exceed 0.05%. These results correspond to the cylindrical specimens located close to the gas inlet. Additionally, in previous work [12], it has been demonstrated that this set of parameters yield fully-dense HX when spatter redeposits are not detected. A stripe scan strategy was used, with 67° rotation between adjacent stripes. The parts were exposed in an optimized manner in relation to the flow of inert gas, with the first parts exposed being furthest away from the gas inlet. The gas flow settings were kept constant in all three builds. After completion of the builds,



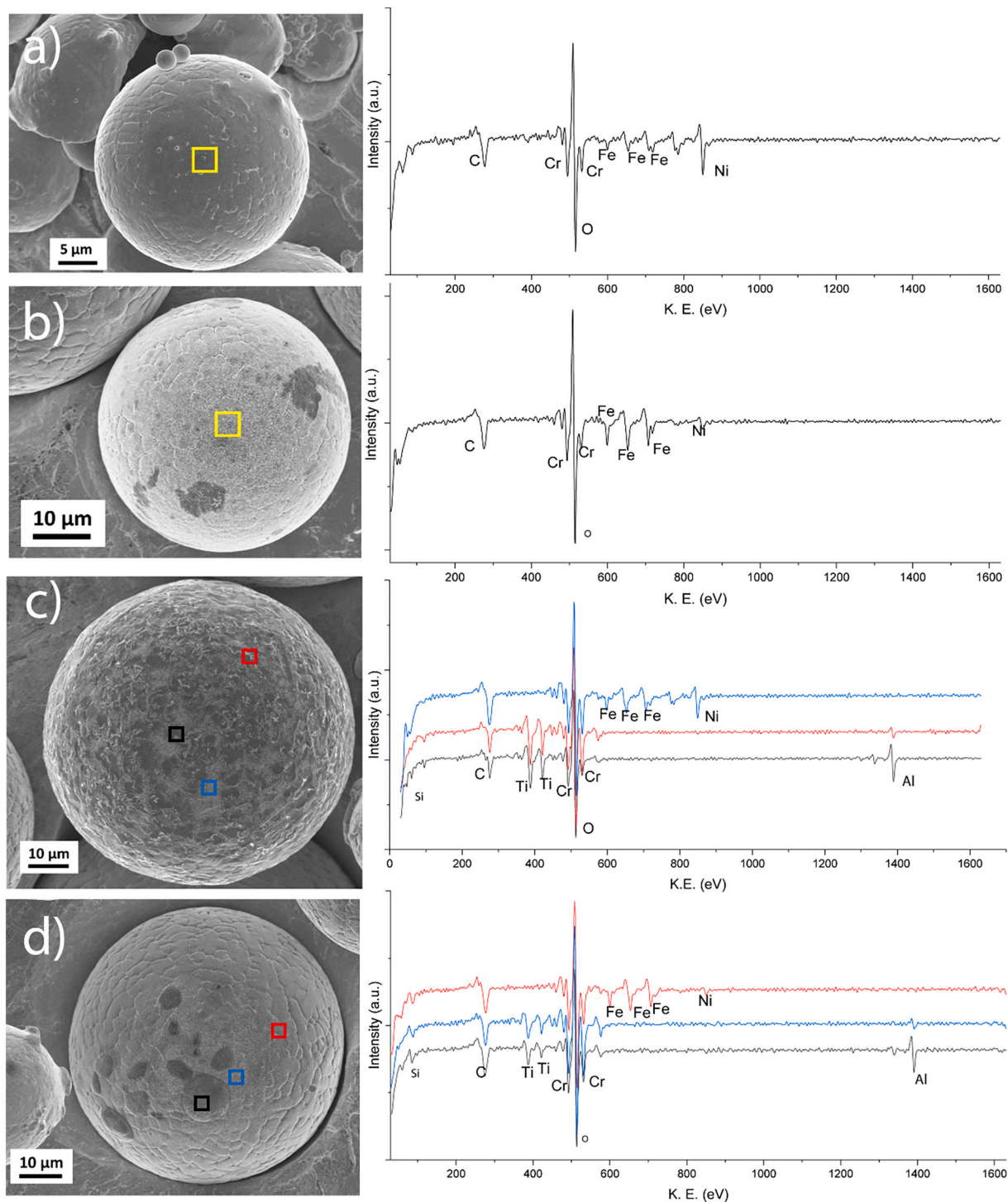


Fig. 7. A comparison of AES analysis of a) virgin and b), c), and d) spatter particles.

spatter samples were carefully collected from the top of the gas outlet, which is the machine component from which the gas exits the build chamber, as described in previous work in detail [10].

The builds were monitored via the EOSTATE Exposure OT tool (EOS GmbH Electro Optical Systems). In this monitoring system, an sCMOS (scientific Complementary Metal–Oxide–Semiconductor) camera is used in conjunction with bypass filters that limit the acquisition to a narrow band of the near-infrared spectrum ( $900 \text{ nm} \pm 12.5 \text{ nm}$ ). The signal is acquired continuously with an exposure time of 0.1 s. During the manufacturing of a build layer, the registrations are combined to output the maximum signal registered in each  $250 \mu\text{m} \times 250 \mu\text{m}$  patch of the

build area, which corresponds to a pixel in the output image (MAX output in EOSTATE Exposure OT). Distortion corrections and noise reduction are applied, and the output is one  $2000 \times 2000$ -pixel greyscale image of the entire powder bed area per manufactured layer. The images can be exported in 16-bit format, meaning each pixel assumes a value ranging from 0 to 65,535, according to its radiation emissions during signal acquisition. The pixel intensities are also called grey values (GV). In this study, the OT system was used for data acquisition only; data processing was performed in a Matlab R2019b environment.

To compare the morphology of virgin powder with the spatter samples and navigate the different types of spatter morphologies, high-

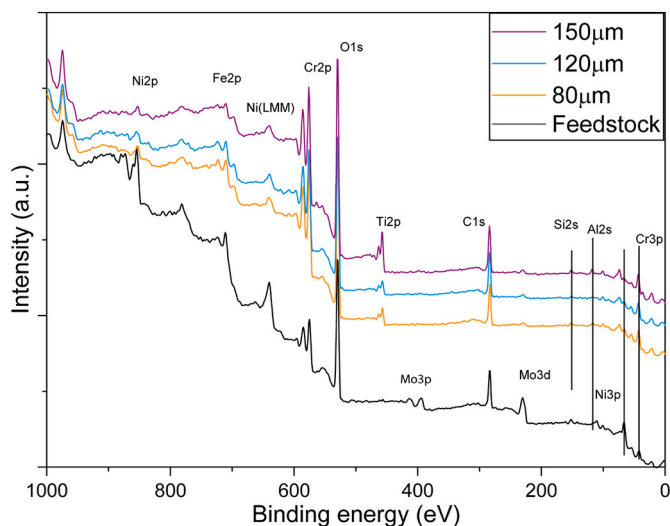


Fig. 8. Comparison of XPS survey spectra from feedstock powder and the spatter samples gathered at 80  $\mu\text{m}$ , 120  $\mu\text{m}$ , and 150  $\mu\text{m}$  layer thickness.

resolution scanning electron microscopy (HR-SEM) using LEO Gemini 1550 was conducted. To observe the variation in surface chemistry, nature of oxides, and oxide layer thickness, X-ray photoelectron spectroscopy (XPS) using a PHI 5500 instrument equipment equipped with a monochromatic Al  $K\alpha$  source was conducted. The powder samples for XPS analysis were mounted on 3 M scotch tape where samples were continuously neutralized using  $\text{Ar}^+$  ions. A large area of  $300\ \mu\text{m} \times 300\ \mu\text{m}$  containing 20–30 particles was analyzed to obtain a statistical average measurement. The thickness of the oxide layer was examined by etching and depth profiling of the samples where  $\text{Ar}^+$  ions were used to etch the powder surface. The etch rate of the instrument was calibrated against  $\text{Ta}_2\text{O}_5$ , therefore, all the oxide thicknesses given here are  $\text{Ta}_2\text{O}_5$  standard units. Auger electron spectroscopy (AES) using a PHI 700 AES from Physical Electronics was done to further investigate the surface chemistry.

### 3. Results and discussion

Fig. 2 shows filled contour plots containing arbitrary identical isolines of the maximum OT signal for a representative layer of each build. As shown in a previous study [12], the scan pattern and laser travel direction determine the direction of travel of spatters, and the amount of spatter ejections can be affected by the building height. Therefore, the layers represented are located at similar build heights with a similar scan pattern for a straightforward visual comparison of the spatter generated in each case. It is observed that, with increasing nominal layer thickness, larger extensions of the build area are affected by signals of the same intensity range (represented by the different colors in Fig. 2). Considering that the gas flow, material, and processing conditions are invariable among builds, and the mechanisms of spatter generation are not expected to vary, equivalent initial temperature, signal emissions, travel velocities, and cooling rates of the process byproducts among builds can be assumed. Consequently, signals of the same intensity range reaching further away indicates that the maximum travel distance is extended as the nominal layer thickness increases. In Fig. 2, it is also noticeable that the signals acquired outside part boundaries, i.e., on projected areas not directly affected by the laser beam, are more intense in equivalent locations concerning distance from the laser exposed area and spatter travel direction. Considering there is an equivalent distribution of temperatures assumed by the spatter particles at any instant, as well as an equivalent distribution of travel speeds on all builds, the detection of signals of higher intensity in equivalent distances from the part boundaries on MAX images indicates that more spatters are generated

on each layer, as this increases the probability of the maximum detected signal being one of higher intensity at any given spot. In conclusion, the OT data suggest that increases in the nominal layer thickness boost the spattering phenomenon on each processing layer.

Fig. 3 shows 3D reconstructions of the three builds from the MAX OT images. The intensity is represented according to the color map indicated. The opacity is proportional to the intensity of the volume rendering. The direction of gas flow is indicated by arrows. All figures are generated with the same parameters. As the nominal layer thickness increases, signals of higher peak intensity are acquired outside part boundaries. Since the conditions for the generation, cooling and traveling of spatters are invariable among builds, this observation can be explained by the generation of a larger number of spatters per layer. As more spatter particles are generated per layer, there is a higher probability to obtain signals of higher intensity at any given location. The MAX OT images highlight the peak intensities, and the three-dimensional reconstructions reveal a consistent scaling of spattering with nominal layer thickness throughout the build process.

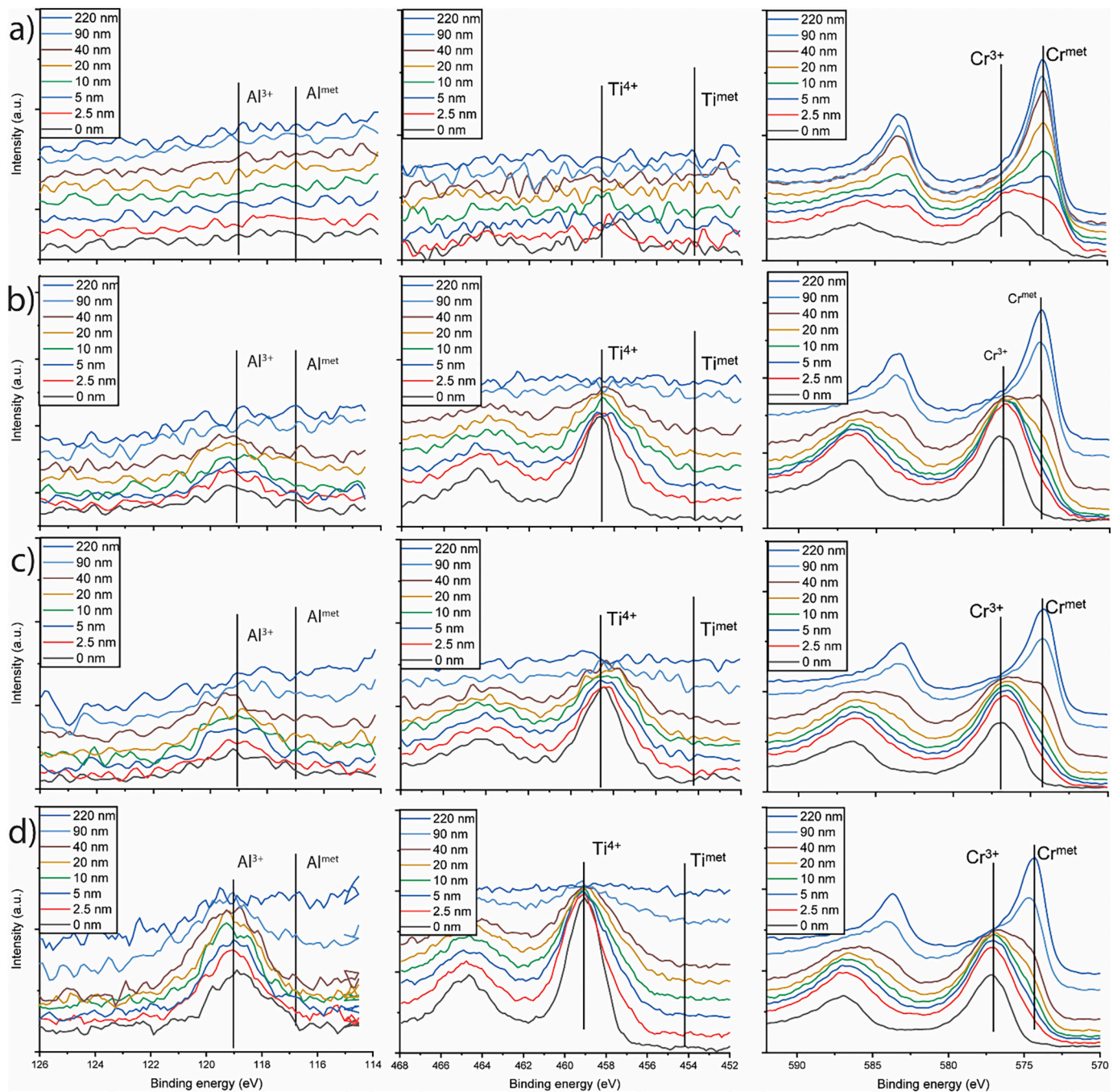
The consequence of layer-wise boosting spattering is an increase in the accumulation of detected spatter particles on the build area, preferentially close to the gas outlet. The deposited particles manifest in the OT monitoring system output as bright blobs, and their detection can be automated [12], as illustrated in Fig. 4, where each indication is circled in red on one representative layer per build. The deposition of spatter particles on the build area has been shown to provoke the formation of a lack of fusion defects [12].

Fig. 5 shows the morphology comparison of virgin powder with the spatter particles collected at varying powder layer thicknesses. The comparison elucidates that the majority of spatter particles have a coarser size than D50 of virgin powder and there are particles with a size larger than D90. Moreover, the spatter particles have higher sphericity compared to the virgin powder and lack satellite particle attachment on the surface. The coarser size and higher sphericity of the spatter particle is an indication that spatters particles mainly consist of the molten/partially molten ejecta by melt-laser-powder interaction where the particles solidified during time of flight. The size of spatter particles has a bimodal distribution in all the particle samples as shown in our previously published work [12] and size distribution is not substantially different with changing layer thickness. Moreover, the morphology of spatter generated in different layer thicknesses is not varying greatly from each other and the main difference is the amount of spatter particles detected through the OT system, which is the representation of hot spatters that are likely to oxidize more.

SEM analysis shows that the spatter particles have different surface morphologies and can be divided into three main groups as shown in Fig. 6. Fig. 6a shows a particle where the surface of the particle is covered with fine oxide particulates. The size of this group of particles is rather small compared to other spatters, which is perhaps contributing to higher oxidation stemming from higher surface energy. The morphology of the second type of particles is shown in Fig. 6b, which is showing a web-like pattern of various regions. The surface contains bright and dark contrast regions highlighting the variation in the type of oxides forming on the surface of such particles. Moreover, the third type of particle is showing a different tendency where localized large particulates are forming on the surface of particles, see Fig. 6c. This set of particles has a dendritic structure on the surface like virgin particles which were not present on the surface of other types of particles. To summarize, the nature of oxide morphology varies in spatter particles from fine oxide particulates and oxide patterns to large particulates showing that the surface of spatter particles is extremely oxidized compared to virgin powder. A general quantitative analysis of the spatter samples shows that the amount of second and third types of particles increased with an increase in layer thickness.

AES analysis has been conducted on the surface of spatters to analyze the different types of spatter particles and identify the type of oxide. AES is an interesting technique to analyze the sample with higher axial





**Fig. 9.** XPS depth profile comparison of Al<sub>2s</sub>, Ti<sub>2p</sub>, and Cr<sub>2p</sub> spectra of a) virgin powder with spatter samples collected from build-job with a layer thickness of b) 80  $\mu\text{m}$ , c) 120  $\mu\text{m}$ , and d) 150  $\mu\text{m}$ .

resolution up to  $\sim 10$  nm. The default SEM in the system assists in identifying the point of interest and performing the spectroscopic analysis which is not possible with XPS analysis where the particles cannot be directly observed and the point of interest cannot be identified. Fig. 7 is showing a comparison of AES analysis of virgin powder with different types of spatter particles. Fig. 7a is showing an AES survey spectrum from virgin powder samples where the peaks from Nickel (Ni), Iron (Fe), and Chromium (Cr), which are the main contributing elements in the HX alloy, can be observed along with oxygen and carbon. Taking the virgin spectrum as a reference, spatter samples are showing varying surface compositions. Fig. 7b is showing the first category of small spatter particles covered with particulates on the surface as shown in Fig. 6a. The AES analysis is showing the dominance of Fe alongside Cr on

the surface, whereas the Ni peak has a minimal intensity. The enrichment of Fe and Cr on the surface is indicating the formation of Fe-Cr-based spinel oxide over the surface in the form of fine oxide particulates.

Fig. 7c is showing a comparison of spectra obtained from the particle which has a pattern of oxides over the surface where an area analysis at three different locations on the surface of the particle has been done. The measurements are highlighted with black, blue, and red squares representing areas on top of dark oxide particulate, next to oxide particulate, and white particulates respectively. The AES spectra from the black square is showing the enrichment of Aluminum (Al) and Titanium (Ti) along with Cr indicating that these oxide particulates mainly consist of Al, Ti, and Cr-based mixed oxide. Considering a very small concentration of Al and Ti in HX alloy, this enrichment is signifying preferential



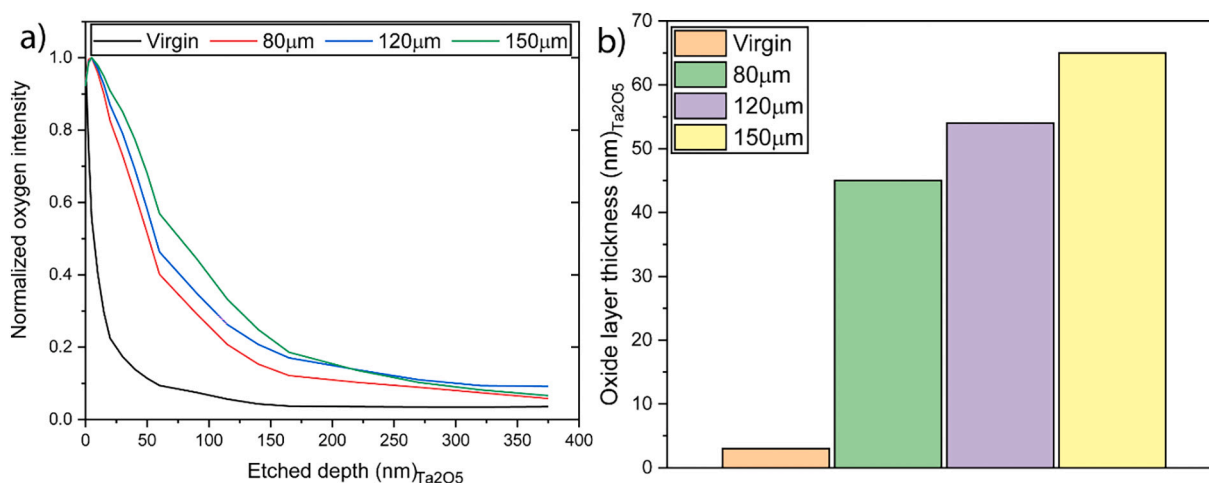


**Fig. 10.** A comparison of a) normalized oxygen intensity w.r.t. etched depth and b) oxide layer thickness of feedstock powder and the spatter samples gathered at 80  $\mu\text{m}$ , 120  $\mu\text{m}$ , and 150  $\mu\text{m}$  layer thickness.

oxidation of the elements with high oxidation susceptibility and diffusivity. The measurement from the area highlighted with a blue square also shows enrichment of Ti and Cr but not as much of Al. Whereas, the spectrum from the red square is showing a composition similar to the one observed on a particle in Fig. 7b.

Lastly, in Fig. 7d, the particle with large oxide particulates has been analyzed and an area analysis at three different locations on the surface of the particle has been done. The tendency is like in the particle shown in Fig. 7c, where the type of oxides varies from one region to the other. Such localized variation in the type of oxides and nature probably stemmed from the difference in temperature exposure and cooling rate locally.

For obtaining a statistical average by analyzing a large number of particles, XPS is a very useful surface-sensitive technique that has been employed in this study. A comparison of XPS survey spectra from as received surface of virgin powder with the spatter samples gathered at different layer thicknesses is presented in Fig. 8. The spectra from feedstock powder is showing peaks from Ni, Cr, Fe, and Mo along with oxygen (O1s) peak, which is highlighting the presence of all the main alloy constituents on the surface of powder in the form of a thin stable oxide layer. Contrarily, in spatter samples, the relative intensity of the peaks from Mo and Ni is very diminished, and the relative intensity of the Cr peak is substantially increased. Moreover, the peaks for alloying elements with a minute concentration in the alloy (e.g., Al and Ti) have appeared in the survey spectra of spatter samples. An increase in the relative intensity of the Cr peak and the appearance of Al and Ti peaks over the surface is indicating surface oxidation of the spatter particles, which is driving the enrichment of oxidation susceptible elements over the surface of spatters.

Enrichment of Al, Ti, and Cr on the surface of spatter samples is further investigated by XPS depth profile analysis to verify the state of these elements, and the thickness of oxides. XPS depth profile analysis is a useful technique of surface analysis where a layer-by-layer surface analysis is conducted by removing the top layer with ion etching. A comparison of narrow scans of Al2s, Ti2p, and Cr2p with varying etch depth from virgin and spatter samples is shown in Fig. 9.

The Al2s spectra from virgin powder in Fig. 9a show a flat line even both in  $\text{Al}^{3+}$  (~119 eV) and  $\text{Al}^{\text{met}}$  (~117 eV) states which represents the low alloying contribution of Al in HX alloy and lack of surface enrichment in virgin powder respectively. However, a peak with a small intensity of 119 eV representing the  $\text{Al}^{3+}$  state can be observed in the analysis of spatter samples. This is an indication of Al enrichment on the surface of particles and forming Al-based oxides. A similar trend can also be observed in Ti2p narrow spectra where no peak was observed both in oxide  $\text{Ti}^{4+}$  (~459 eV) and metal  $\text{Ti}^{\text{met}}$  (~454 eV) states in virgin powder.

However, a surge in peak intensity was observed in the spatter samples at  $\text{Ti}^{4+}$  (~459 eV) highlighting the oxide enrichment on the surface of spatter particles. From the depth profile analysis of the spatter particles, the peaks of both  $\text{Al}^{3+}$  and  $\text{Ti}^{4+}$  can be observed at the depth of 40 nm with no sign of metallic peaks. This is a probable indication of their presence in the particulate form.

Being one of the main alloying elements with the ability to form the stable oxide layer, the Cr2p spectra is showing the presence of Cr-based oxide through a  $\text{Cr}^{3+}$  peak at 476.5 eV on as received virgin powder. However, the oxide thickness is very low which is evidenced by the appearance of the  $\text{Cr}^{\text{met}}$  peak at 474.5 eV after 2.5 nm etching of the as-received surface. Contrary to the virgin powder, the spatter samples are showing extensive surface oxidation as the  $\text{Cr}^{\text{met}}$  peak is appearing after ~40 nm etched depth. To summarize the data from the depth profile analysis, the spatter samples are extensively oxidized compared to the virgin powder, and the oxide particulates consist of Cr along with Al and Ti. The presence of Al and Ti is highlighting the enrichment of these elements from the core of the ejecta particles during solidification/cooling after the ejection by laser-melt-powder interaction.

XPS depth profile analysis can also assist in evaluating the distribution of oxygen in the form of oxide from the surface of the particle to the core which can be used to determine the oxide layer thickness on the surface of the particle, see Fig. 10. Fig. 10a is showing the normalized oxygen intensity of the investigated samples with the etched depth which is estimated from the O1s spectra measured during the analysis. The comparison of spectra shows a sharp decline in normalized oxygen content in the virgin sample with a slight surface etching. However, the tendency is different in the case of spatter samples where the decline is not as sharp. A similar trend has been previously noted in Alloy 718 too where the oxygen persisted at a larger depth in the spatter particles [10,11,13,14]. This illustrates an increase in oxide layer thickness in spatter samples. The comparison of spatters collected from different layers is also showing a trend where an increase in oxygen content with the increase in the thickness of the powder layer.

The oxide layer thickness of virgin powder and spatter samples is measured using O1s spectra, Fig. 10b. The oxide-metal interface is determined using the technique presented by other researchers [15,16]. The result shows a substantial increase from virgin (average oxide layer thickness ~2.5 nm) to spatter samples. The average oxide layer thickness increased with the increase in powder layer thickness in the build job. All the oxide thickness values presented here are calibrated against  $\text{Ta}_2\text{O}_5$  standard foil; therefore, the layer thickness is represented in  $\text{Ta}_2\text{O}_5$  units and actual thickness values may slightly vary depending on the etch rate of different oxides.

To evaluate the possibility of the formation of different types of

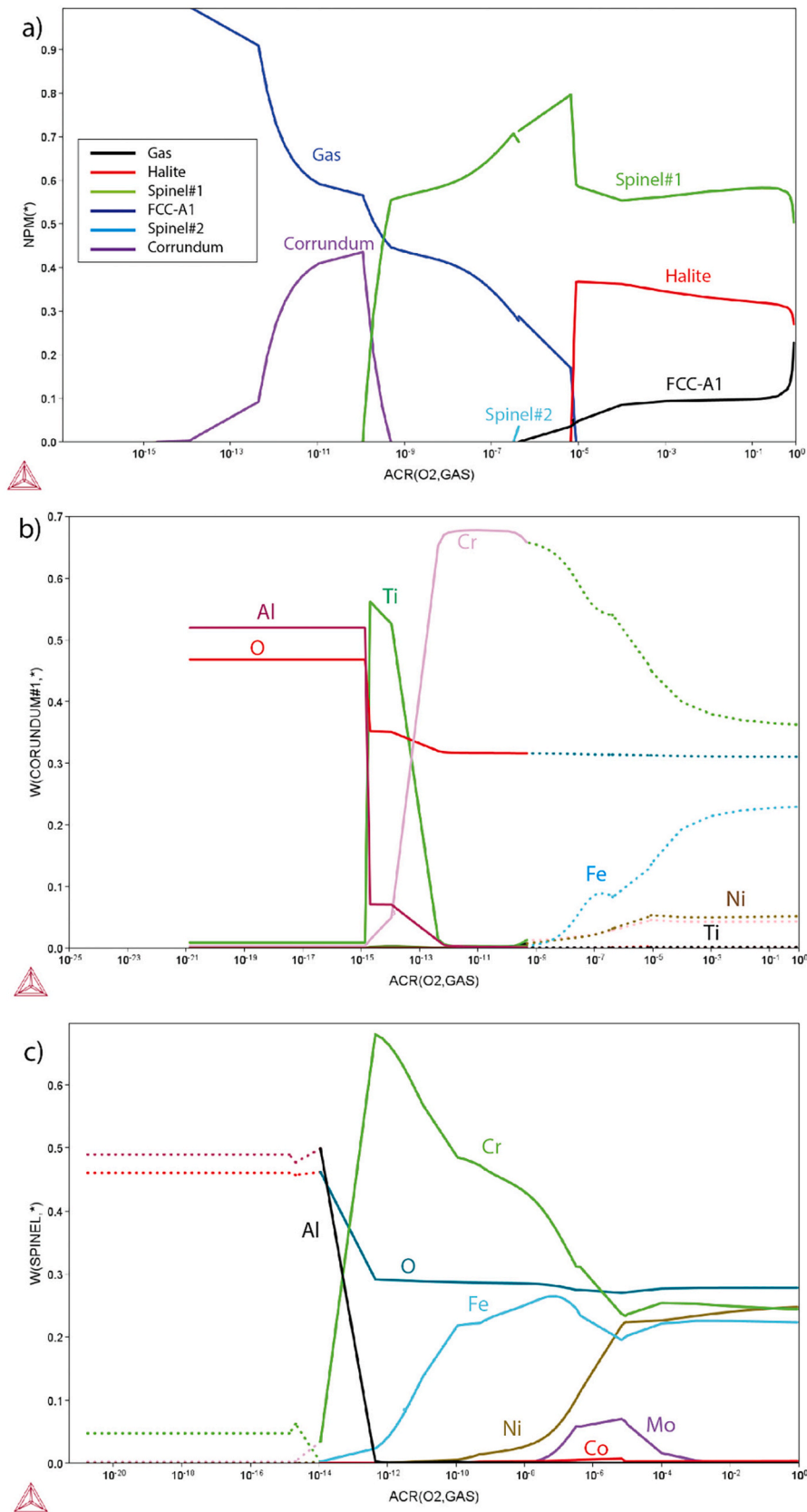


**Fig. 11.** Thermodynamic calculations using Thermo-Calc 2021: (a) equilibrium phase fraction at 1500°C with varying oxygen partial pressure, (b) composition of corundum 1 phase, and (c) composition of spinel phase. The dashed lines correspond to the elemental compositions in the metastable phase.

oxides, observed in spectroscopy analysis considering the thermodynamics, calculations were performed using Thermo-Calc software (2021a, CTOX10 database). The results from morphology analysis show that the oxidized spatters, particularly the first and the second type of spatters shown in Fig. 6, are missing virgin-like dendritic structure on the surface of the particles which is an indication of melting and re-solidification of the spatters ejected from the melt pool. Therefore, the calculations are done at 1500 °C which is substantially higher than the usual melting point for HX alloys (1316 °C).

Fig. 11a shows the calculated phase composition of HX alloy at 1500 °C with varying oxygen partial pressure. At lower oxygen partial pressure, a corundum phase forms. Fig. 11b illustrates the variation in the composition of the corundum phase where it is enriched with Al-based oxides at a lower partial pressure of oxygen. The Cr and Ti enrichment in the spinel phase occurs at higher oxygen partial pressure. The phase composition also shows a transition of phases from corundum to spinel with a slight increase in oxygen activity, where the spinel phase is dominantly enriched with Cr and Fe. Here, it is important to highlight that the printing and spatter generation process was done at an oxygen level of 1000 ppm ( $10^{-3}$ ) where the formation of the corundum phase enriched with Al- and Ti-based oxides can be ruled out. However, the experimental results have shown the formation of the Al- and Ti-rich phases on the surface of spatter samples. This is probably linked to the non-equilibrium nature of spatters solidification and cooling, which is causing a localized depletion of oxygen and enrichment of Al- and Ti-based oxides. Therefore, the corundum phase, which only forms at extremely low oxygen partial pressure, is forming on the surface of the spatter particles.

#### 4. Conclusion

In this work, a comprehensive surface analysis has been done to relate the effect of powder layer thickness on the extent of spatter oxidation. The in-situ monitoring system (OT system) was used to investigate the effect of powder layer thickness on the generation of spatter particles during the processing of HX alloy. The following conclusions can be drawn from the findings of this paper:

- In-situ monitoring revealed that as the nominal layer thickness increases:
  - o The maximum travel distance of the spatter particles is extended;
  - o A larger number of spatter particles is generated per each layer;
  - o A larger number of spatter particles are deposited on the powder bed, leading to the formation of a lack of fusion defects.
- As the monitoring was performed in a layer-wise manner, it was possible to observe the consistency of these observations throughout the build processes.
- The SEM analysis of the spatters indicates that the spatter can be divided into three groups depending on the surface morphology of the particles. AES analysis elucidated that the nature and composition of oxides on the surface of the spatter particles vary from each other where the surface of some spatter particles are enriched with Al and Ti-based oxides and others are forming Fe and Cr-based oxide spinel phase.
- The XPS analysis highlighted that the surface enrichment of various oxide-forming elements varied with the layer thickness. The enrichment of Al- and Ti-based oxides was lowest in the spatters generated at 80 µm, and it scaled with the nominal powder layer thickness.
- The average oxide layer thickness also increased with powder layer thickness from ~2.5 nm in virgin, ~45 nm in 80 µm, ~55 nm in 120 µm, and ~68 nm in 150 µm powder layer thickness spatter sample.
- Thermo-Calc calculations further supported the experimental findings, where Al and Ti-rich corundum and Fe and Cr-rich spinel formation was evident.

The increase in the amount of spatters generated with powder layer thickness observed through the in-situ monitoring system is pointing towards an increase in the number of hot spatters (as the OT system detects heat signals). Such hot spatters have higher oxidation susceptibility, which is confirmed through surface analysis. Hence, the OT system can be a useful technique to qualitatively investigate the extent of powder degradation.

#### CRedit authorship contribution statement

**Ahmad Raza:** Conceptualization, Methodology, Investigation, Formal analysis, Visualization, Writing – original draft. **Claudia Schwerz:** Conceptualization, Investigation, Formal analysis, Writing – original draft. **Camille Pauzon:** Investigation, Formal analysis, Writing – review & editing. **Lars Nyborg:** Resources, Supervision, Writing – review & editing. **Eduard Hryha:** Conceptualization, Methodology, Funding acquisition, Project administration, Supervision, Writing – review & editing.

#### Declaration of Competing Interest

The authors declare that they have no known competing financial interests or personal relationships that could have appeared to influence the work reported in this paper.

#### Data availability

Data will be made available on request.

#### Acknowledgment

This work was conducted within the framework of the Centre for Additive Manufacturing – Metal (CAM2), supported by the Swedish Governmental Agency of Innovation Systems (Vinnova), and of the project MANUELA - Additive Manufacturing using Metal Pilot Line, funded by European Union's Horizon 2020 Research and Innovation Programme under grant Agreement no. 820774. The authors would like to thank Electro Optical Systems Finland Oy for providing the feedstock powder utilized in this research.

#### Appendix A. Supplementary data

Supplementary data to this article can be found online at <https://doi.org/10.1016/j.powtec.2023.118461>.

#### References

- [1] P. Paradise, D. Patil, N. Van Handel, S. Temes, A. Saxena, D. Bruce, A. Suder, S. Clonts, M. Shinde, C. Noe, D. Godfrey, R. Hota, D. Bhate, Improving productivity in the laser powder bed fusion of Inconel 718 by increasing layer thickness: effects on mechanical behavior, *J. Mater. Eng. Perform.* (2022), <https://doi.org/10.1007/s11665-022-06961-8>.
- [2] A. Leicht, M. Fischer, U. Klement, L. Nyborg, E. Hryha, Increasing the productivity of laser powder bed fusion for stainless steel 316L through increased layer thickness, *J. Mater. Eng. Perform.* 30 (2021) 575–584, <https://doi.org/10.1007/s11665-020-05334-3>.
- [3] Z. Sun, X. Tan, S.B. Tor, W.Y. Yeong, Selective laser melting of stainless steel 316L with low porosity and high build rates, *Mater. Des.* 104 (2016) 197–204, <https://doi.org/10.1016/j.matdes.2016.05.035>.
- [4] C. Schwerz, F. Schulz, E. Natesan, L. Nyborg, Increasing productivity of laser powder bed fusion manufactured Hastelloy X through modification of process parameters, *J. Manuf. Process.* 78 (2022) 231–241, <https://doi.org/10.1016/j.jmapro.2022.04.013>.
- [5] S. Wang, Y. Liu, W. Shi, B. Qi, J. Yang, F. Zhang, D. Han, Y. Ma, Research on high layer thickness fabricated of 316L by selective laser melting, *Materials (Basel)* 10 (2017), <https://doi.org/10.3390/ma10091055>.
- [6] C. de Formanoir, U. Paggi, T. Colebrants, L. Thijs, G. Li, K. Vanmeensel, B. Van Hooreweder, Increasing the productivity of laser powder bed fusion: influence of the hull-bulk strategy on part quality, microstructure and mechanical performance of Ti-6Al-4V, *Addit. Manuf.* 33 (2020), 101129, <https://doi.org/10.1016/j.addma.2020.101129>.



- [7] C. Qiu, C. Panwisawas, M. Ward, H.C. Basoalto, J.W. Brooks, M.M. Attallah, On the role of melt flow into the surface structure and porosity development during selective laser melting, *Acta Mater.* 96 (2015) 72–79, <https://doi.org/10.1016/j.actamat.2015.06.004>.
- [8] T. Fiegl, M. Franke, A. Raza, E. Hryha, C. Körner, Effect of AlSi10Mg0.4 long-term reused powder in PBF-LB/M on the mechanical properties, *Mater. Des.* 212 (2021), 110176, <https://doi.org/10.1016/j.matdes.2021.110176>.
- [9] A. Raza, T. Fiegl, I. Hanif, A. Markström, M. Franke, C. Körner, E. Hryha, Degradation of AlSi10Mg powder during laser based powder bed fusion processing, *Mater. Des.* 198 (2021), 109358, <https://doi.org/10.1016/j.matdes.2020.109358>.
- [10] C. Pauzon, A. Raza, E. Hryha, P. Forêt, Oxygen balance during laser powder bed fusion of alloy 718, *Mater. Des.* 201 (2021), <https://doi.org/10.1016/j.matdes.2021.109511>.
- [11] A. Raza, C. Pauzon, E. Hryha, A. Markström, P. Forêt, Spatter oxidation during laser powder bed fusion of alloy 718: dependence on oxygen content in the process atmosphere, *Addit. Manuf.* 48 (2021), 102369, <https://doi.org/10.1016/j.addma.2021.102369>.
- [12] C. Schwerz, A. Raza, X. Lei, L. Nyborg, E. Hryha, H. Wirdelius, In-situ detection of redeposited spatter and its influence on the formation of internal flaws in laser powder bed fusion, *Addit. Manuf.* 47 (2021), 102370, <https://doi.org/10.1016/j.addma.2021.102370>.
- [13] Z. Chen, A. Raza, E. Hryha, Influence of part geometry on spatter formation in laser powder bed fusion of Inconel 718 alloy revealed by optical tomography, *J. Manuf. Process.* 81 (2022) 680–695, <https://doi.org/10.1016/j.jmapro.2022.07.031>.
- [14] L. Cordova, A. Raza, E. Hryha, Rheological behavior of Inconel 718 powder for electron-beam melting, *Metals* 12 (2022) 1231.
- [15] E. Hryha, R. Shvab, M. Bram, M. Bitzer, L. Nyborg, Surface chemical state of Ti powders and its alloys: effect of storage conditions and alloy composition, *Appl. Surf. Sci.* 388 (2016) 294–303, <https://doi.org/10.1016/j.apsusc.2016.01.046>.
- [16] C. Oikonomou, D. Nikas, E. Hryha, L. Nyborg, Evaluation of the thickness and roughness of homogeneous surface layers on spherical and irregular powder particles, *Surf. Interface Anal.* 46 (2014) 1028–1032, <https://doi.org/10.1002/sia.5439>.